Integrating Materials and Manufacturing Innovation (2019) 8:318–334
https://doi.org/10.1007/s40192-019-00149-0

THEMATIC SECTION: ADDITIVE MANUFACTURING BENCHMARKS 2018

Elastic Residual Strain and Stress Measurements and Corresponding Part Deflections of 3D Additive Manufacturing Builds of IN625 AM-Bench Artifacts Using Neutron Diffraction, Synchrotron X-Ray Diffraction, and Contour Method

Thien Q. Phan[1] · Maria Strantza[2] · Michael R. Hill[3] · Thomas H. Gnaupel-Herold[4] · Jarred Heigel[1] · Christopher R. D'Elia[3] · Adrian T. DeWald[5] · Bjorn Clausen[2] · Darren C. Pagan[6] · J. Y. Peter Ko[6] · Donald W. Brown[2] · Lyle E. Levine[7]

Received: 10 May 2019 / Accepted: 9 July 2019 / Published online: 29 July 2019

Abstract
One of the primary barriers for adoption of additive manufacturing (AM) has been the uncertainty in the performance of AM parts due to residual stresses/strains. The rapid heating and cooling rates from the thermal history of the laser melting process result in high residual stresses/strains that produce significant part distortion. Efforts to mitigate residual stresses using post-process heat treatments can significantly impact the microstructures of the AM part which may lead to further issues. Therefore, the ability to accurately predict the residual stresses in as-built AM parts is crucial, and rigorous benchmark measurements are needed to validate such predictions. To fill this need, the AM-Bench aims to provide high-fidelity residual stress and strain benchmark measurements in well-characterized AM bridge-shaped parts. The measurements reported here are part of the residual elastic strain benchmark challenge CHAL-AMB2018-01-RS. Residual strains and stresses in this work were measured using neutron diffraction, synchrotron X-ray diffraction, and the contour method. Part deflection measurements were performed using a coordinate measurement machine after the part was partially separated from the build plate. These independently measured results show a high degree of agreement between the different techniques.

Keywords Additive manufacturing · Residual stress · Neutron diffraction · Synchrotron X-ray diffraction · Contour method · Nickel-based superalloy

Introduction

The presence of high residual stress in engineering alloy components produced by additive manufacturing (AM) is one of the challenges that must be solved before wide spread adoption of AM. Residual stresses and strains are inherently linked to the processing conditions. For the laser powder bed fusion (LPBF) process, the thermal gradients, cooling rates, and part mechanical constraints result in the multi-length-scale residual stresses that exist within the as-built part [1–5]. These stresses can affect the component life in service and cause a catastrophic failure during the build such as part separation from the build plate. As such, there exists a need to validate and improve the accuracy of model predictions for residual stresses. The AM-Bench measurement series was established to develop rigorous benchmark

✉ Thien Q. Phan
thien.phan@nist.gov

1 Engineering Laboratory, National Institute of Standards and Technology, Gaithersburg, MD 20899, USA

2 Los Alamos National Laboratory, Los Alamos, NM 87545, USA

3 Mechanical and Aerospace Engineering, University of California, Davis, CA 95616, USA

4 NIST Center for Neutron Research, National Institute of Standards and Technology, Gaithersburg, MD 20899, USA

5 Hill Engineering, LLC, Rancho Cordova, CA 95670, USA

6 Cornell High Energy Synchrotron Source, Ithaca, NY 14853, USA

7 Materials Measurement Laboratory, National Institute of Standards and Technology, Gaithersburg, MD 20899, USA

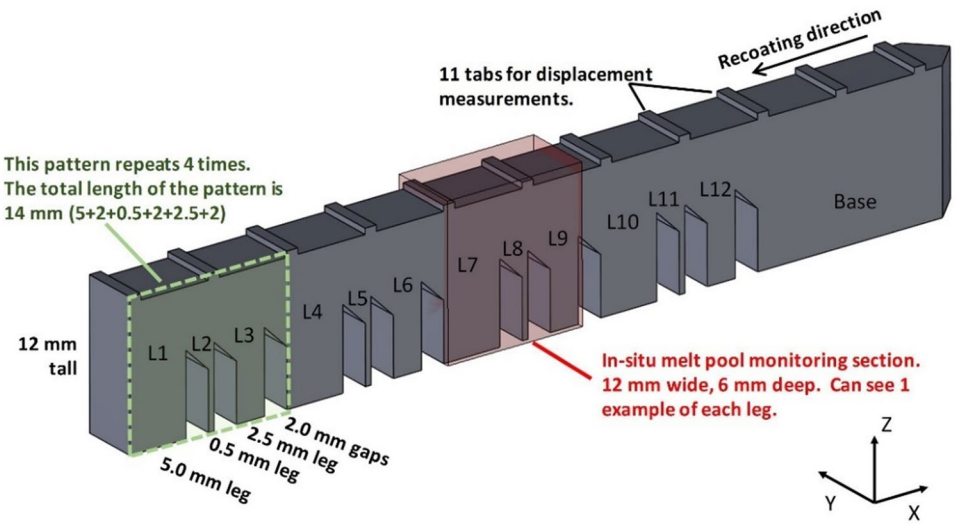

Fig. 1 The AMB2018-01 bridge structure geometry shown here without the attached build plate. The strain/stress measurements were performed on parts still attached to the build plate

measurements for all AM materials and methods. A description of how these residual stress measurements fit into this larger picture is given in the introductory article to this topical collection [6].

In this work, multiple measurement methods were used to measure the elastic residual strains and stresses within AM samples made from Inconel 625 (IN625), a solid solution hardened nickel-based super alloy. Additional measurements on 15-5 steel AM-Bench specimens will be reported in a later publication. Both destructive and nondestructive methods were used. In addition, the distortion effects of these residual strains and stresses were characterized by measuring part deflections that occurred after partially separating the AM part from the build plate. Detailed measurement results may be found on the National Institute of Standards and Technology (NIST) AM-Bench website, at www.nist.gov/ambench/benchmark-test-data under AMB2018-01: residual elastic strains, and AMB2018-01: part deflection.

Experimental Procedure

The IN625 feedstock powders used for building the AM-Bench parts were obtained from the same powder lot from EOS[1] and kept sealed in the original shipment containers until use. Virgin powder feedstock was used for all samples measured in this work. Particle size distribution (PSD) and chemical composition analysis were performed on powder samples collected and riffled. The PSD measurements were performed using a commercial dynamic image analysis system. Chemical compositions were measured using mass spectroscopy performed at two external laboratories. Chemical composition measurements follow ASTM E1019. Detailed results of the PSD and composition can be found on the NIST AM-Bench website, at www.nist.gov/ambench/amb2018-01-description.

The AMB2018-01 tests consist of AM LPBF 3D metal alloy builds of a bridge structure geometry with 12 legs of varying size, as shown in Fig. 1. The bridge-shaped structures were additively produced from virgin IN625 powder using an EOS M270[1] system with modifications for in situ measurements. The 12 legs consist of 4 replications of a section described in the green box in Fig. 1. Each section consists of 3 distinct leg sizes: 5 mm, 0.5 mm, and 2.5 mm. The AM parts were built on build plates of nominally the same alloy (IN625) as shown in Fig. 2. The build plates were 100 mm squares with 12.7 mm thickness, mounted to the middle of the build area of the LPBF machine.

The bridge-shaped structures were built using the nominal parameter set for IN625. The contour laser power and scan speed were 100 W and 900 mm/s, respectively, and the infill laser power and scan speed were 195 W and 800 mm/s, respectively, with a hatch distance spacing of 100 µm. The build consisted of a total of 625 layers, with a 20-µm layer height. According to the manufacturer, the D4σ laser diameter on the build plane is 85 µm during the contour scans, but defocuses to 100 µm for the infill scans. For the infill scans, the laser paths alternate between motion along the x-axis for odd number layers and along the *y*-axis for even layers. The part designs, build plate, build layouts, scan strategy, and scan parameters are further detailed on the AM-Bench website and another manuscript (Heigel et al., unsubmitted). For residual stress/strain measurements, four (4) bridge-shaped

[1] Mention of commercial products does not imply endorsement by the National Institute of Standards and Technology, nor does it imply that such products or services are necessarily the best available for the purpose.

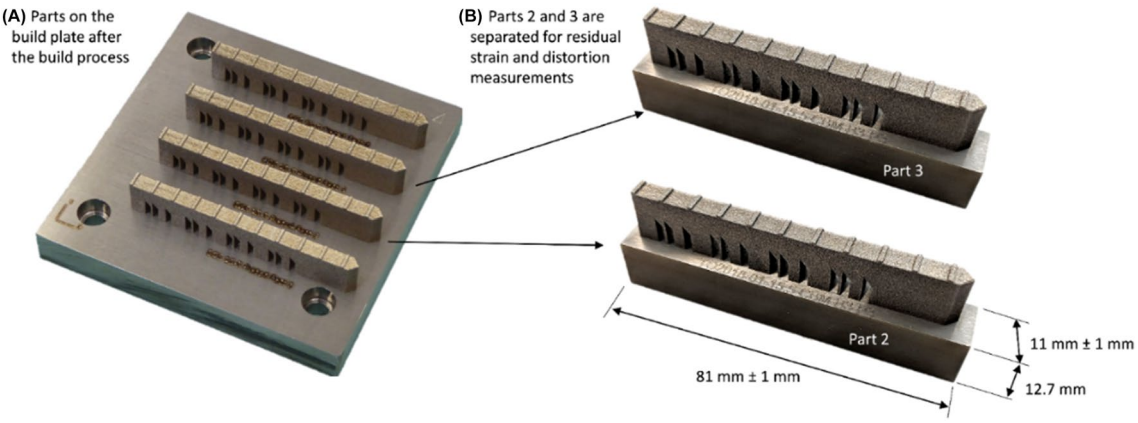

Fig. 2 **a** Four bridge structures were built on a build plate of the same nominal chemical composition (IN625). **b** Parts were separated using wire EDM with the build plate attached for residual strain and distortion measurements after the build process

parts were built on a build plate as shown in Fig. 2. After the build was completed, each part including the surrounding attached build plate was separated from other parts using wire electric discharge machining (EDM). All residual stress/strain measurements were performed on individual sections extracted from the initial build plate. Each section included the part still attached to a portion of the build plate (as shown in Fig. 2b). The parts were measured in the as-built condition. Figure 2a shows the build plate with 4 parts attached after the build process and (B) the separation of two of the parts after the build process.

The residual elastic strains within the as-built IN625 parts were measured using neutron diffraction on the BT8 diffractometer at the NIST Center for Neutron Research (NCNR), energy-dispersive synchrotron X-ray diffraction at the ID1A3 beamline at the Cornell High Energy Synchrotron Source (CHESS), and the contour method at University of California, Davis, and Hill Engineering, LLC. Part deflection was measured using a coordinate measurement machine (CMM) at NIST.

Neutron Diffraction Measurements

Neutron diffraction measurements were performed at the NCNR using the BT8 diffractometer. The measurement procedures are similar to those reported in previous works [7, 8]. Measurements were performed in monochromatic mode, using a neutron beam with a wavelength of approximately $\lambda = 0.1537$ nm. The measured gauge volume is approximately cubic (1.5 mm × 1.5 mm × 1.5 mm) and is defined by the incident and diffracted beam slits. This cube size represents the nominal spatial resolution of the measurements. It is worth noting that the edges of the gauge volumes are not parallel to the XYZ coordinate axes. Instead, the cubic volume is rotated by 45° about the Z axis.

Figure 3 shows the center positions of the diffraction measurement volumes; the axes and origin are indicated in the figure. Measurements were performed in the X–Z plane at $Y = 2.5$ mm (mid-plane). The positions are broken into two sections: the top sections and the bottom/legs sections. The top section consists of a grid of 3×43 positions (rows × columns) in the Z and X directions, respectively. The position spacings are 1.464 mm in the Z direction and 1.4 mm in the X direction. The first measurement column is positioned at $X = 1$ mm, and the top measurement row is at $Z = 11$ mm (1 mm from the side and top edges). The bottom/leg measurements are composed of 5 subsections; each is a 5×3 grid (rows x columns), with the same spacings as the top section in the X and Z directions, respectively. The leg measurements were aligned with the top measurement section to keep the positions and spacings of the measurement consistent. No measurements were performed in the medium and thin leg sections due to the large neutron gauge volume. No measurements were made in the large solid section of the part. A total of 204 positions were measured for three components (X, Y, and Z directions) of elastic strain.

The lattice spacings of the (311) reflection were used for the strain determination. The lattice spacings along the X, Y, and Z orientations for the locations described above were measured by orienting and moving the sample with respect to the neutron beam using translation/rotation goniometer stages. The diffraction angle (2θ) between the diffracted beam and the incident beam is approximately 90°. Figure 4 shows the sample orientations and movements with respect to the neutron beam for measurement of strain components along the X, Y, and Z directions.

Neutron diffraction data were collected for 10 min to 60 min per strain component (3 components total) per measurement position, depending on texture and neutron path through the sample. The diffraction peak was then

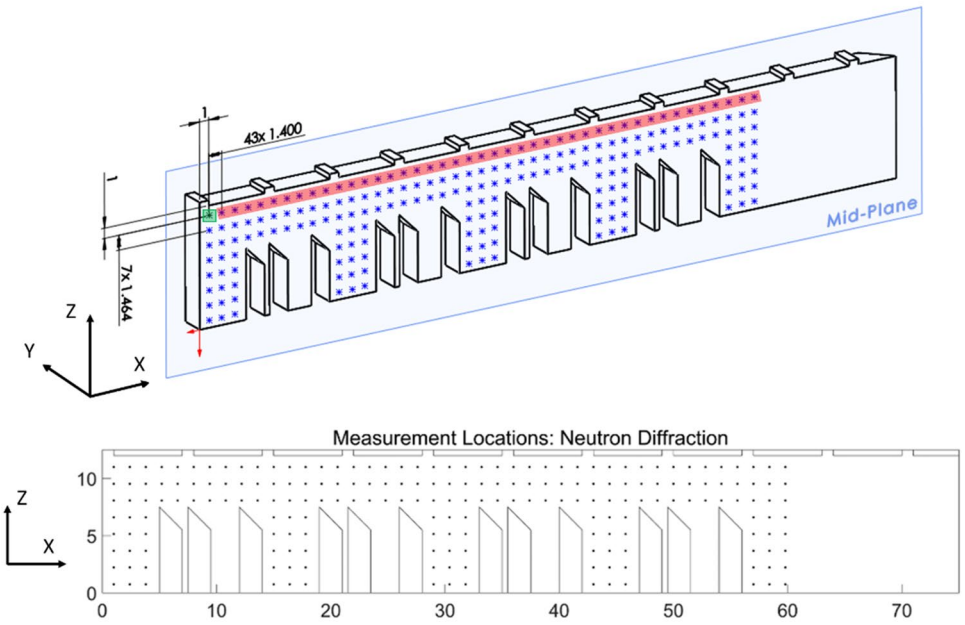

Fig. 3 Neutron diffraction measurement center locations for residual elastic strains. Both axes show distances in the *X* and *Z* directions in mm. All strain values are averaged over cubic volumes (1.5 mm × 1.5 mm × 1.5 mm). Measurement locations are spaced 1.4 mm apart in the *X* direction, and 1.464 mm apart in the *Z* direction

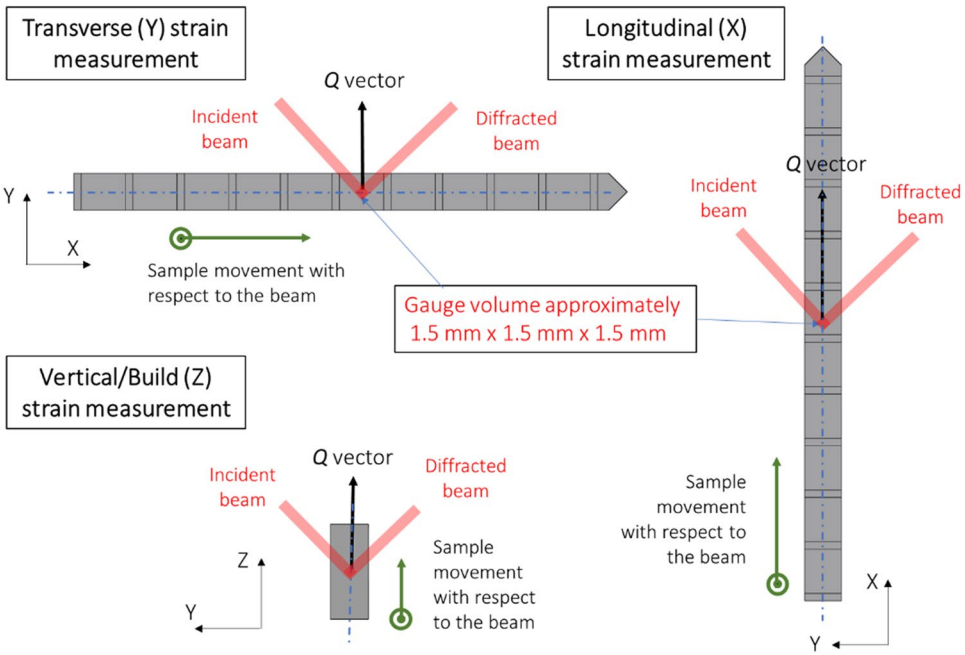

Fig. 4 Neutron diffraction residual strain measurement setup. The Q-vector bisects the angle between the incident beam and the diffracted beam. The Q-vector points along the direction of the strain component measured

fitted using a Gaussian distribution and the lattice spacing (d_{311}) calculated. Once the lattice spacings were obtained, elastic strains could be calculated based on an unstressed lattice parameter (d_0). This d_0 was obtained by applying a stress-free boundary condition for near surface measurements, specifically $\sigma_{zz} = 0$ (perpendicular to the surface) along the top 42 measurement positions (highlighted in red in Fig. 3), or $\sigma_{zz} = \sigma_{xx} = 0$ at the top corner position (highlighted in green in Fig. 3). The basic equation used is described by Eq. 1:

$$\varepsilon(hkl, \varphi, \psi) = \frac{d(hkl, \varphi, \psi) - d_0}{d_0} = F_{ij}(hkl, \varphi, \psi)\sigma_{ij} \quad (1)$$

This equation simply states that the (*hkl*)-dependent lattice strain, ε, measured in a direction given by the spherical polar angles (φ, ψ) is the sum of strain contributions

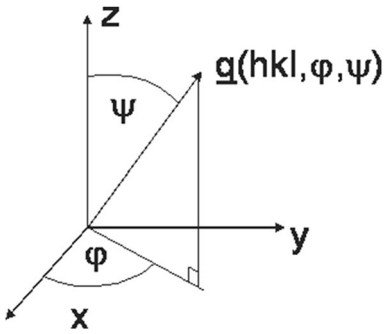

Fig. 5 Coordinate system used in neutron diffraction. The vector $\mathbf{q}$ defines the measurement direction

from all stress tensor components σ_{ij} (multiplied by the diffraction elastic constants $F_{ij}(hkl, \varphi, \psi)$). Note that the F_{ij} depend on the reflection (hkl) as well as the measurement direction (φ, ψ). Figure 5 defines the neutron diffraction angles.

Here, the diffraction elastic constants F are calculated from the single-crystal elastic constants of IN625: $C_{11} = 243.6$ GPa, $C_{12} = 156.7$ GPa, and $C_{44} = 117.8$ GPa [9] using IsoDEC [10]. For each location where $\sigma_{zz} = 0$ applies, there are *three* equations of this kind (one d-spacing for each orientation measured) forming a system that can be solved for the *three* unknowns (σ_{xx}, σ_{yy}, and d_0). Equation 1 can be used to obtain explicit expressions (Eq. 2) for the three orthogonal measurement directions: $X = (0°, 90°)$, $Y = (90°, 90°)$, and $Z = (0°, 0°)$:

$$\varepsilon_{xx} = \frac{d_x - d_0}{d_0} = F_{xx}(0°, 90°)\sigma_{xx} + F_{yy}(0°, 90°)\sigma_{yy} + F_{zz}(0°, 90°)\sigma_{zz} \tag{2a}$$

$$\varepsilon_{yy} = \frac{d_y - d_0}{d_0} = F_{xx}(90°, 90°)\sigma_{xx} + F_{yy}(90°, 90°)\sigma_{yy} + F_{zz}(90°, 90°)\sigma_{zz} \tag{2b}$$

$$\varepsilon_{zz} = \frac{d_z - d_0}{d_0} = F_{xx}(0°, 0°)\sigma_{xx} + F_{yy}(0°, 0°)\sigma_{yy} + F_{zz}(0°, 0°)\sigma_{zz} \tag{2c}$$

Once the d_0 is calculated, the elastic strain components for all measured positions were calculated. This same system of equations can be used for the location where $\sigma_{zz} = \sigma_{xx} = 0$.

Energy-Dispersive X-Ray Diffraction Measurements

Energy-dispersive diffraction measurements were conducted on part 2 (Fig. 2) on the ID1A3 beamline at the Cornell High Energy Synchrotron Source (CHESS). The ID1A3 beamline utilizes a continuous spectrum incident X-ray beam with effective spectrum from 40 keV to 200 + keV, which corresponds to a wavelength of 0.0248 nm to 8.2656×10^{-3} nm. Previous efforts by others have utilized energy-dispersive X-ray diffraction for high-resolution residual strain mapping of large engineering samples [11–13]. The procedures and experimental setup in this work are similar to measurements performed on AM-built Ti–6Al–4V bridge-shaped structures [14]. The incident X-ray beam was masked to a 0.25 mm × 0.25 mm cross section by a pair of incident beam slits, made out of a high-density tungsten-based alloy HD17 [15]. The beam penetrated the sample and diffracted through two sets of receiver slits with a fixed angle (2θ) of 9.18° to a germanium, single element Canberra GL-0055 energy-resolved detector. The multiple slit geometry results in a "rhomboidal"-shaped diffraction volume of 0.25 mm × 1.5 mm × 0.25 mm, where the extended dimension is approximately along the Y direction of the sample (inset in Fig. 6).

The sample was positioned in a four-circle goniometer with built-in translation stages. Individual diffraction patterns were collected from the X–Z cross section at $Y = 2.5$ mm (mid-plane of the sample). The setup enabled the automated positioning and rotation of the sample to collect data for the orthogonal strain components along X and Z, as well as the strain component of the 45° off Z direction. It should be mentioned that it was not possible to determine the Y-strain component because the necessary sample orientation results in an X-ray path length of 75 mm. The X-ray absorption through 75 mm of IN625 made it impossible to measure the residual strain for the Y component. Figure 6 shows the energy-dispersive X-ray diffraction setup for measurements along the X, Z, and 45° off Z directions.

The measurement locations for the lattice strains are illustrated in Fig. 7. The measurements were conducted 0.25 mm from the edges of the sample. However, on the regions close to the "taper" side of the sample the measurements were performed 0.75 mm from the edge of the chevron. The measurement grid spacing is divided into two parts: the large solid section with a spacing of 1 mm and the leg sections with a spacing of 0.5 mm.

Unlike the neutron measurements of the current work, where only the lattice spacing along one family of planes (311) was measured, energy-dispersive X-ray diffraction collects the entire X-ray line pattern for each measurement position and direction. A total of 6777 1-D diffraction patterns were collected and refined using the automated SMARTSware [16] and general structural analysis system (GSAS) [17] software for multiple peak fitting to derive the best strained unit cell parameter. The unstrained lattice parameter a_0 was obtained by measuring a separate small reference sample (2 mm × 2 mm × 3 mm) extracted via EDM from a nominally identical AM build to ensure that no macroscopic residual stress exists [18]. Strain values ε_i along a given Q direction

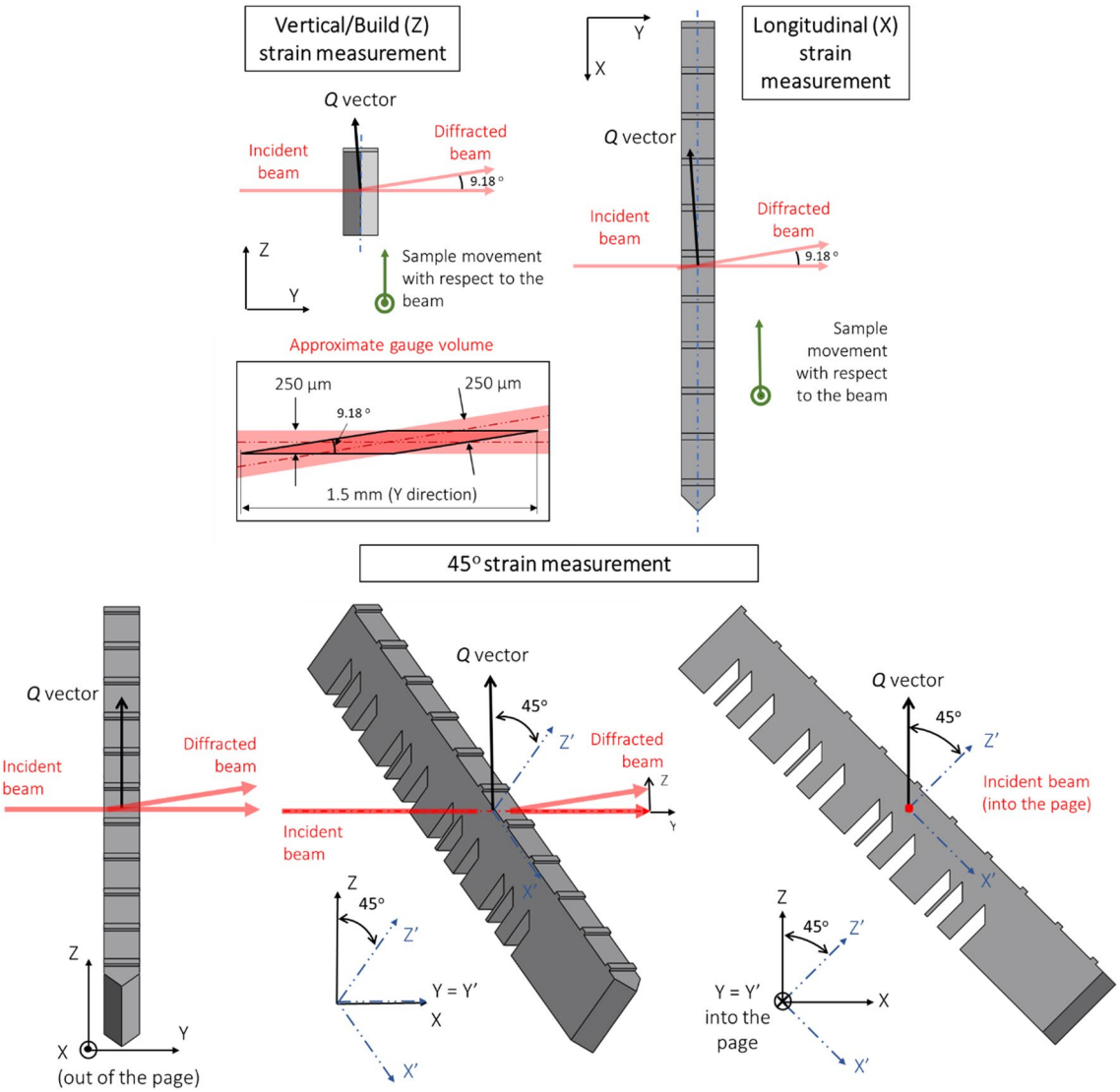

Fig. 6 Energy-dispersive X-ray diffraction measurement setup for the *Z*, *X*, and 45° directions. The diffracted beam is 9.18° away from the incident beam. The Q-vector points approximately 4° along the direction of the strain component measured

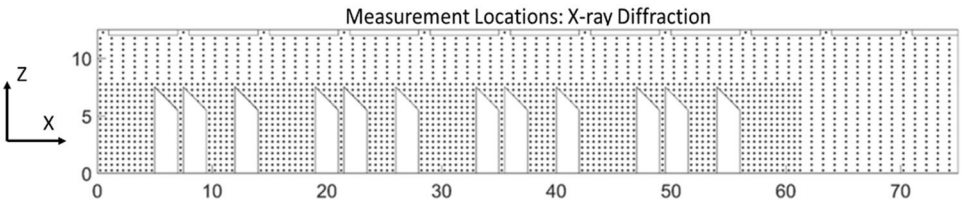

Fig. 7 Measurement locations for the residual strains measured using synchrotron X-ray diffraction at the ID1A3 beamline at the Cornell High Energy Synchrotron Source (CHESS)

were found by fitting a cubic unit cell parameter a to the entire X-ray intensity spectrum and then calculating ε_i as:

$$\varepsilon_i = \frac{a_i - a_0}{a_0} \tag{3}$$

Contour Method Measurements

In addition to the nondestructive measurements using neutron and X-ray diffraction, residual stresses were measured on a separate bridge-shaped AM-Bench sample using the contour method, a mechanical stress release technique [19]. The contour method was used to measure the longitudinal

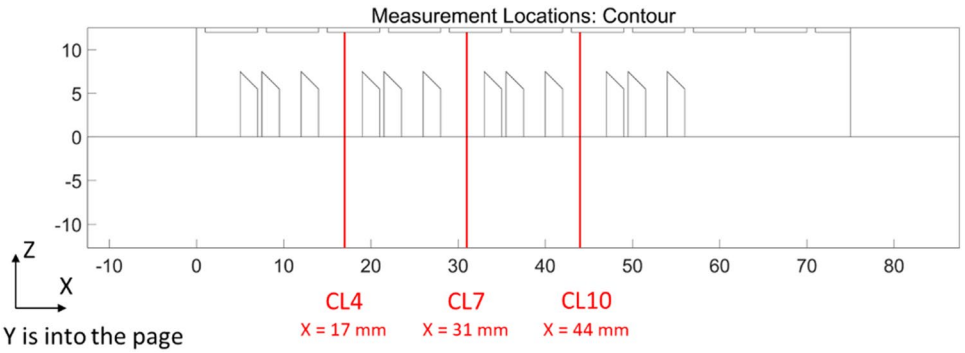

Fig. 8 Measurement locations for the residual stress measured using the contour method (contour leg 7 = CL7). EDM sectioning was performed at $X = 17$ mm, 31 mm, and 44 mm marked CL4, CL7, and CL10. Note that the contour method sections the attached part and baseplate, allowing for the stress measurement through the baseplate

(X) residual stress at three planes, each bisecting one of the 5-mm-wide legs CL4, CL7, and CL10, as shown by the red lines in Fig. 8.

The contour method provides a two-dimensional map of the spatial variation of residual stress normal to the measurement plane. A first step in the contour measurement was to section the part on the plane of interest using wire EDM. The cut surfaces are deformed from flat plane by the release of residual stress, and a second step is to measure the two-dimensional surface profiles of each half of the cut using a scanning profilometer. The profile measurements had in-plane point spacing of 0.25 mm and a height resolution of 0.001 mm. The two cut surface profiles were analyzed to remove noise (roughness) and retain their form (shape), and then the forms of each half of the cut surface pair were averaged together to eliminate the effects of shear stress and cut path variation. The negative of the smoothed, average surface form is finally used as a displacement boundary condition in a linear elastic stress analysis to estimate the residual stress as a function of position on the cut plane. Elastic material properties used for the contour stress analysis were: 207 GPa for the elastic modulus and 0.278 for the Poisson's ratio [20]. Further description of the contour method is available in the literature [19].

The contour measurements required an extension beyond a typical measurement because the measurement planes are not planes of geometric symmetry. Drawing on the prior work of Mahmoudi [21], the extension consisted of performing two stress analyses, each using geometry of one half of the cut part (i.e., one analysis for the left side of the cut part and a second for the right side) with the final measured stress being the average of the results from the two stress analyses.

Part Deflection Measurements

Another AM sample was used to measure the vertical part deflection. Before any measurements were performed, the tops of the 11 ridges were ground to provide smooth surfaces that could be accurately measured with a coordinate measuring machine (CMM) at NIST. The CMM used in this study has an International Organization for Standardization (ISO) 10360-2 maximum permissible error (MPE) of 5 µm. The height of the ground surfaces of each ridge relative to the top surface of the baseplate was calculated from three measurements made across the ridge and two measurements made on the baseplate, on either side of the part. Figure 9a illustrates the locations of the 55 CMM measurements and the reference point for the CMM measurements. After the first CMM measurements, the 12 legs were then separated from the baseplate via EDM, allowing the part to deflect upward (positive Z direction) due to the release of residual stress, as shown in Fig. 9b. The CMM measurements were performed a second time to measure the new relative height between the ridges and baseplate. Part deflection was calculated by the difference between these two sets of measurements.

Results and Discussion

Unstrained Lattice Parameter and Uncertainty Analysis

Inherently, diffraction techniques measure lattice spacings. Measured lattice spacings for samples that exhibit residual strains will be the *strained* plane spacings. The unstrained lattice spacing (d_0) is often determined using a stress-free boundary condition, whether directly near a free surface on the sample being measured, or on a separate specimen extracted from the large sample.

For the neutron diffraction measurements in this work, the d_0 is determined from the measured lattice spacings near free surfaces of the sample. The unstrained lattice *parameter* (a_0) is calculated from the unstrained lattice *spacing* (d_0 of the 311 reflection) and presented for ease of comparison to X-ray results. Unstrained lattice parameters (a_0) were calculated along the 43 positions near the top of the sample according to [10]. The a_0 calculated from the 42 positions near the top of the sample (highlighted in red in Fig. 3) is $0.35803\ \text{nm} \pm 0.0004\ \text{nm}$, with the uncertainty reported as the 1 standard deviation. The a_0 calculated from the corner

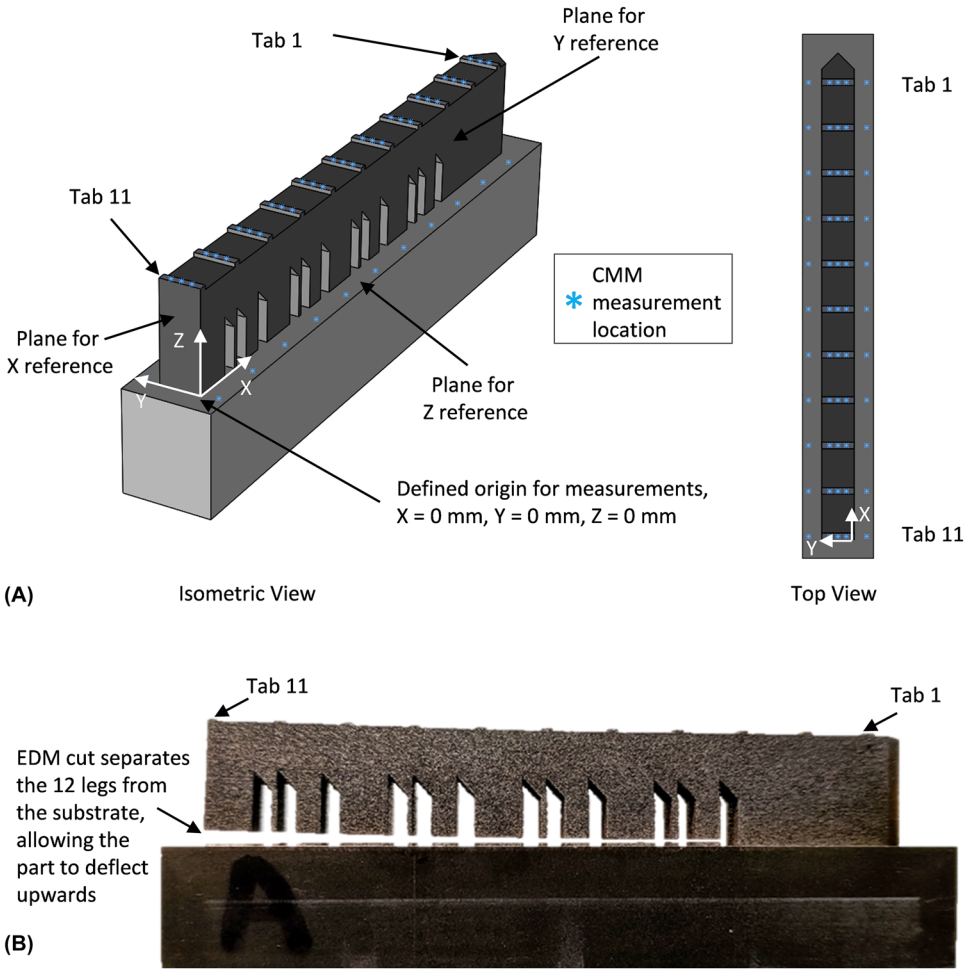

Fig. 9 **a** Illustration of the CMM measurement points and the defined origin for the measurements. **b** Part deflection after the legs are separated from the baseplate via EDM

position measurements (highlighted in green in Fig. 3) is 0.35820 nm ± 0.00012 nm, with uncertainty reported from the statistical peak fitting of diffraction data. The difference between these a_0 measurements (top versus corner positions) translates to approximately 4.7×10^{-4} strain (approximately 60 MPa in stress) and is about 4 times higher than the 1 σ in the 42 top measurements. The a_0 calculated from the corner measurement ($a_0 = 0.35820$ nm) was used for the residual strain calculations due to the location having 2 stress-free surfaces. Note that the choice of top edge versus corner a_0 effectively shifts all the calculated elastic strains and stresses an equal amount and will affect the residual strain values equally at all measurement locations. This means that the choice of a_0 will only change the magnitude, but not the trend (variations) of the residual strain maps reported. The average strain uncertainty determined by statistical peak fitting of the collected neutron diffraction measurement data is approximately 6.7×10^{-5}.

For X-ray diffraction, a_0 was measured from a smaller cube extracted from a reference sample via EDM (2 mm × 3 mm × 3 mm). The a_0 measurement setup is similar to the X-ray diffraction measurement setup described earlier. A total of 25 values for a_0 were measured along the longitudinal (X) and vertical/build (Z) directions and averaged to be 0.35909 nm with a standard deviation of 0.00006 nm. This one standard deviation in a_0 translates to approximately 1.7×10^{-4} in strain. Note that the unstrained lattice parameter values measured using neutron and X-ray diffraction are slightly different. This is due to the inherent differences between the measurement setups. Both instruments are used for strain measurements rather than absolute lattice parameter determination. Since strain is the difference between measured lattice spacings, the systematic error is canceled out when strain is calculated. Figure 10 shows the results of the synchrotron X-ray a_0 measurements. These measurements show very small variations in lattice parameter from the edge to the interior of the cube. This confirms that very little macroscopic residual stress exists within the small sample and the a_0 measured value is appropriate for use as an unstrained lattice parameter.

The experimental uncertainties of the X-ray measured strain values are approximately 1×10^{-4} and are derived from the statistical estimated standard deviations of the Rietveld peak fitting.

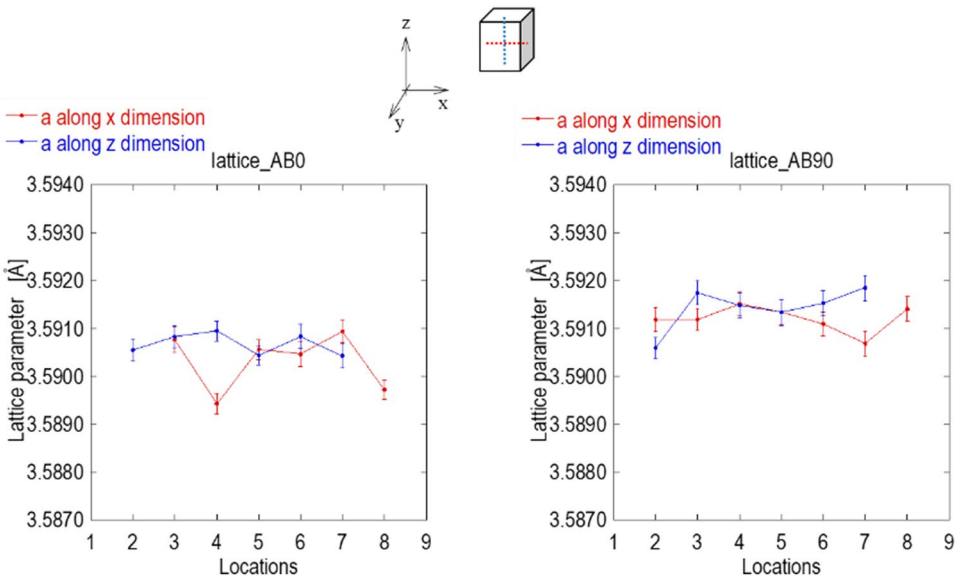

Fig. 10 Unstrained lattice parameter (a_0) measurements of the reference AM sample

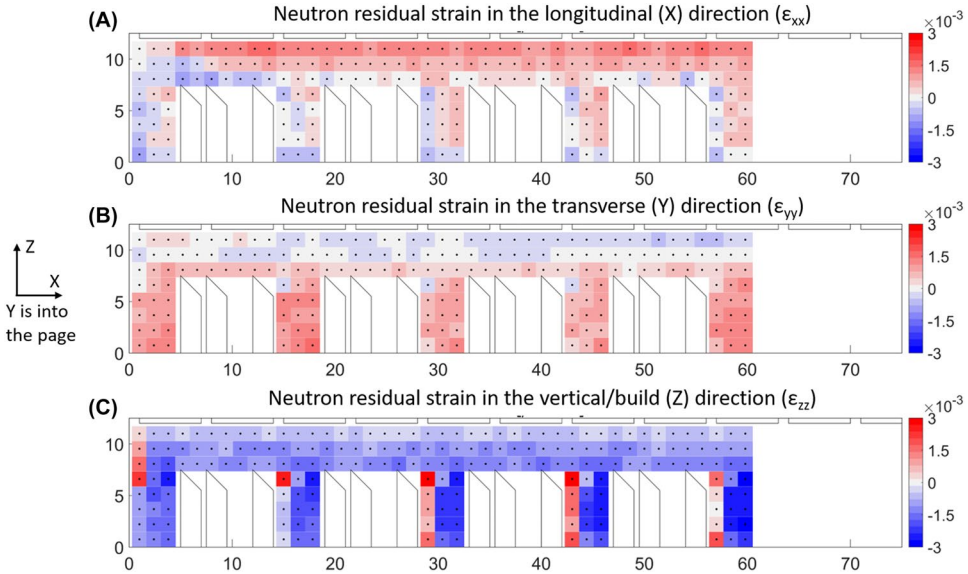

Fig. 11 Residual strain maps of the as-built AM IN625 sample measured using neutron diffraction. Measurements were made in the middle cross section of the sample ($Y = 2.5$ mm) of the **a** longitudinal (X) strain, **b** transverse (Y) strain, and **c** vertical/build (Z) strain. The X and Z positions are shown in mm. Systematic uncertainty in strain associated with the choice of the unstrained lattice parameter is approximately 4.7×10^{-4}. Statistical uncertainty in strain associated with the peak fitting is approximately 6.7×10^{-5}

Neutron Elastic Strain Measurements

The results in this work will be presented by using a two-dimensional pseudo-color representation of the X–Z plane of the sample. The residual elastic strains from neutron diffraction along the X, Y, and Z directions were calculated using Eq. 2 for all measurement positions and plotted as residual strain maps. Figure 11 shows the neutron diffraction-measured residual strain components along the longitudinal (X), transverse (Y), and vertical/build (Z) directions of the AM IN625 sample. The solid black dots indicate the centers of each measurement position. Positive (tensile) strain values are shown in red, and negative (compressive) strain values are shown in blue.

Longitudinal (X) strains near the top of the sample remain mostly positive. This indicates that the top section of the sample is under tension along the X (longitudinal) direction. Residual strains in the vertical/build (Z) directions are mostly negative, indicating a compressive strain state, except for regions very near the left edges of the sample and legs. Due to the gauge volume size, only three measurement columns were performed along the X direction within each large leg. These three columns within the four legs are aligned with the top measurement positions and are not centered within the legs. Residual strains vary from positive (red) to negative (blue) from the left side to the right side of the legs. This variation will be further discussed and verified by comparing with higher-resolution X-ray diffraction results. Note that neutron

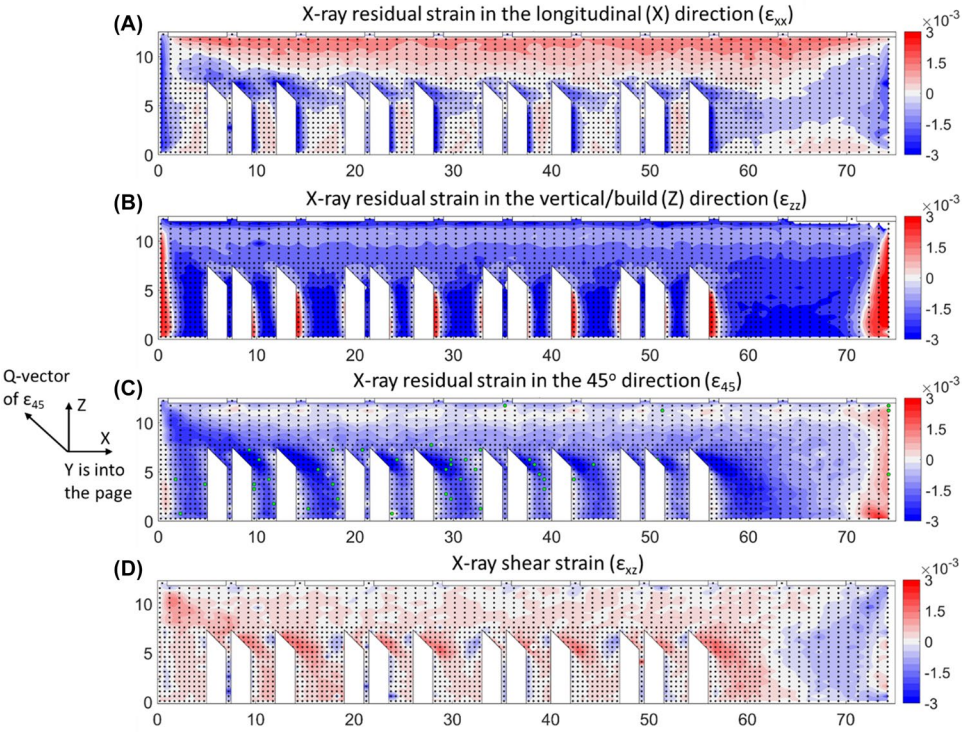

Fig. 12 Residual strain maps of the as-built AM IN625 sample measured using synchrotron X-ray diffraction. Measurements were made in the middle cross section of the sample ($Y = 2.5$ mm) of the **a** longitudinal (X) strain, **b** the vertical/build (Z) strain, **c** the strain at 45°, and **d** calculated tensorial shear strain (ε_{xz}). The X and Z positions are shown in mm. The aqua colored circles of **c** show the locations where the Rietveld refinement failed due to data quality issues. The one standard deviation in the measured unstrained lattice parameter translates to approximately 1.7×10^{-4} in strain. Statistical uncertainty in strain associated with the Rietveld peak fitting is approximately 1×10^{-4}

diffraction-measured strain values are calculated based on the measured lattice plane spacings *averaged* over the measurement volume (1.5^3 mm^3). Neutron strain results therefore cannot show variations over length scales smaller than the size of the measurement volume and will smooth out short length-scale strain variations.

X-Ray Elastic Strain Measurements

Figure 12 shows the X-ray diffraction elastic strains, including (A) the longitudinal (X) strain (ε_{xx}), (B) vertical/build (Z) direction strain (ε_{zz}), (C) the strain at 45° off Z (ε_{45}), and (D) the tensorial shear strain (ε_{xz}). The tensorial shear strain component (ε_{xz}) was calculated using Eq. 4:

$$\varepsilon_{xz} = \frac{1}{2}\left(\varepsilon_{xx} + \varepsilon_{zz}\right) - \varepsilon_{45} \tag{4}$$

Figure 12b shows that the Z strain component of the residual strain is compressive through the interior of the sample, ranging between -3.2×10^{-3} and -9×10^{-4} while the sides of the sample exhibit high-tensile regions (3×10^{-4} to 3.5×10^{-3}). On the other hand, Fig. 12a shows that the X strain components are mostly tensile. The maximum tensile values are present closer to the top and the bottom of the sample. The tensile region concentrated at the top of the sample (6×10^{-4} to 2×10^{-3}) causes a bending moment that will drive the distortion of the sample when the sample is released from the substrate. Moreover, Fig. 12c shows that the strain at 45° is mainly compressive, ranging between -3×10^{-3} and -2×10^{-4} with a thin tensile region close to the taper side of the sample. The results of the calculated tensorial shear strain are also shown in Fig. 12d. It is important to mention that according to the shear definition, at the locations where the shear components are not zero, the principal strain axes do not align with the coordinate axes of the sample.

Contour Method Measurement Results

Figure 13 shows contour method residual stress results for leg 7 (CL7 = contour leg 7) including the stress fields computed on each half of the cut part and their average. The small differences in the three fields suggest that part asymmetry about the cut plane had only a small effect on the measurement.

Contour method results for all three planes, CL4, CL7, and CL10 are shown in Fig. 14. The residual stresses in all legs are similar, being tensile at the top of the build and at the build free surfaces, and compressive at the build center and in the upper half of the baseplate. The overall character of the stress field shows that the build has a net bending moment of one sign (tension at the build top, compression at the build bottom) that is balanced by an opposing bending

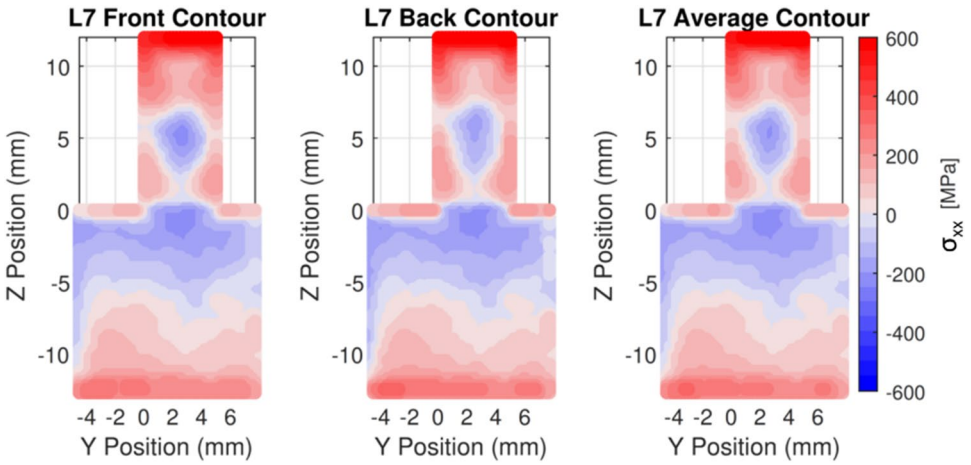

Fig. 13 Maps of longitudinal (*X*) residual stresses from the contour method in CL7; average stress at right is computed as described in the text

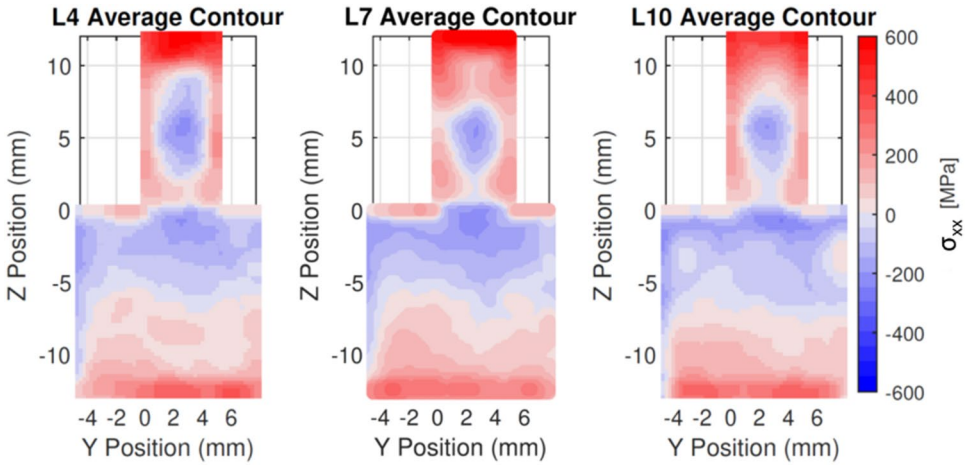

Fig. 14 Maps of longitudinal (*X*) residual stresses from the contour method in CL4, CL7, and CL10

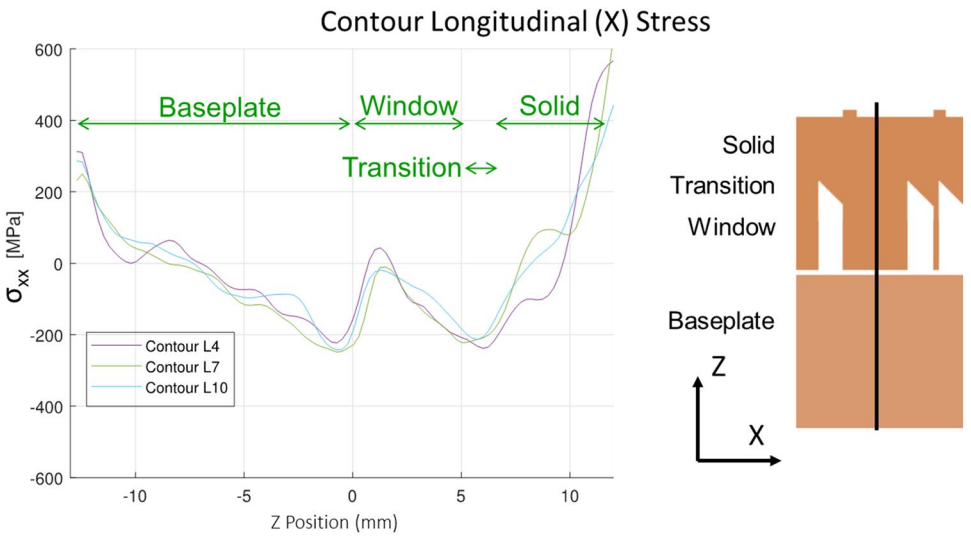

Fig. 15 Line plot of the longitudinal (*X*) residual stresses from the contour method at the center plane of CL4, CL7, and CL10. The figure on the right shows the associated baseplate, window, transition, and solid regions on the sample. A rough estimate of the stress uncertainty measured by the contour method is less than 50 MPa [22]

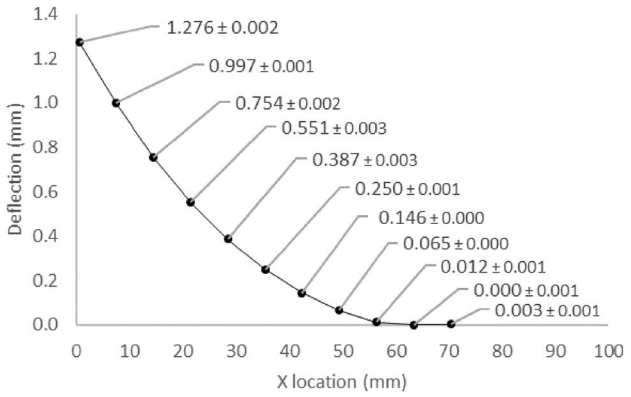

Fig. 16 Deflection measurements of the AM IN625 bridge part after the legs are separated from the baseplate via EDM

moment in the baseplate (tension at the plate bottom, compression at the plate top).

The line plot in Fig. 15 allows for a quantitative comparison of the contour results in the different legs as a function of vertical position at the center of the build width ($Y = 2.5$ mm) with text notations showing areas along the height including the baseplate, the area above the baseplate where there are windows through the build (gaps between legs), where the windows transition to the solid upper portion of the build, and the solid region. Features of the stress field exhibit transitions at locations that correspond to these different geometric features.

Deflection Measurements

Deflection results calculated from the CMM measurements are presented in Fig. 16. The label on each point reports the average of the deflection calculated from the 3 measurement points across each ridge and the standard deviation of those values. We emphasize that these uncertainties are strictly statistical from a limited number of measurements and do not include the CMM MPE of 0.005 mm. Deflection measurements are all positive, indicating upward deflection of the part after separation from the build plate via EDM. The deflection results suggest tensile longitudinal residual stresses on the top of the part, in agreement with the neutron and X-ray residual stress measurements. No systematic twist of the separated specimen was observed.

Comparison

Residual Stress Comparison Between Contour Method and Neutron Diffraction

Three orthogonal (311) lattice plane spacing measurements made using neutron diffraction in the longitudinal (X), transverse (Y), and vertical or build (Z) directions were used to calculate residual stresses as described above. Neutron longitudinal (X) residual stresses were calculated for positions in the mid-plane ($Y = 2.5$ mm) near leg 4, 7, and 10 ($X = 17$ mm, 31 mm, and 44 mm) to compare with contour

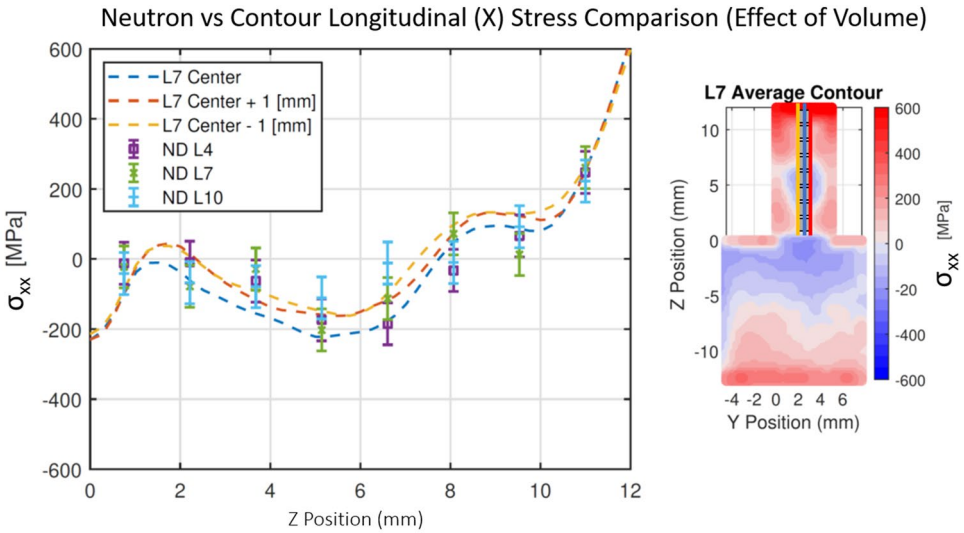

Fig. 17 Longitudinal (X) stress comparison between contour method and neutron diffraction measurements. Line profiles of residual stresses in the longitudinal (X) direction from the contour method for L7 at $X = 31$ mm are plotted for $Y = 1.5$ mm, 2.5 mm, and 3.5 mm. Neutron (ND) longitudinal residual stresses are plotted as markers for L4, L7, and L10. The gray boxes on the figure (right) show approximate locations and sizes of the neutron gauge volumes. The yellow, blue, and red vertical lines on the figure (right) indicate the locations of the contour residual stress line profiles on the graph (left). A rough estimate of the stress uncertainty measured by the contour method is less than 50 MPa [22]. Error bars for the stress measurements by neutron diffraction are systematic errors determined by the choice of the unstrained lattice parameter

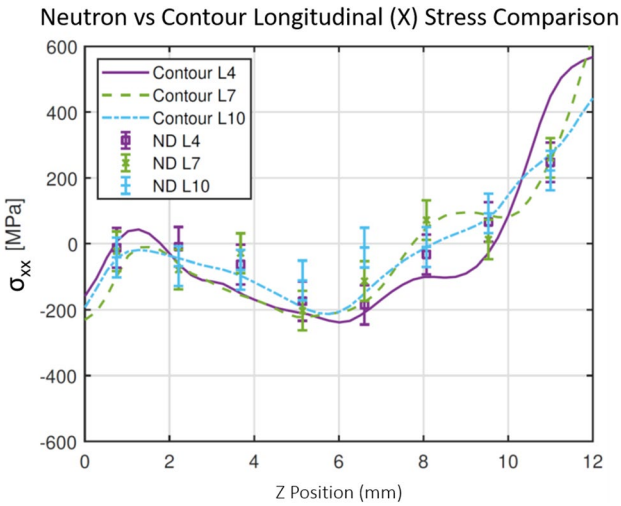

Fig. 18 Longitudinal (X) stress comparison between contour method and neutron diffraction measurements. Line profiles of residual stresses in the longitudinal (X) direction from the contour method are plotted at the mid-plane ($Y=2.5$ mm) for L4, L7, and L10. Neutron (ND) longitudinal residual stresses are plotted as markers for L4, L7, and L10. A rough estimate of the stress uncertainty measured by the contour method is less than 50 MPa [22]. Error bars for the stress measurements by neutron diffraction are systematic errors determined by the choice of the unstrained lattice parameter

results at leg 7 (L7) ($X=31$ mm). To examine the averaging effect of the neutron gauge volume, contour results are plotted at the edges and centers (in the Y positions) of the neutron gauge volumes in Fig. 17.

The cubic neutron gauge volumes for the longitudinal (X) residual stress measurements are oriented such that the cross section of the Y–Z plane with the gauge volume is a rectangle, approximately 1.5 mm × 2.1 mm in the Z and Y directions, respectively. Figure 17 shows the line profiles of the contour method longitudinal (X) stresses at L7 along three (Z) lines at $Y=1.5$ mm, 2.5 mm, and 3.5 mm. These are near the left edge, center, and right edge of the neutron measurement volumes. Neutron results for L4, L7, and L10 are plotted using markers. Since neutron measurements were only performed above the build plate, only results above $Z=0$ mm are plotted and compared. Longitudinal (X) residual stresses vary from near zero, to mildly compressive in the middle heights, to highly tensile near the top of the part. Values from neutron and contour methods show a high degree of agreement except near the extreme positions (top and bottom) of the part, where neutron diffraction has insufficient spatial resolution to capture the extreme stress gradients. The contour results show approximately −200 MPa at $Z=0$ mm and 600 MPa at $Z=12$ mm. Due to the size and averaging effect of the gauge volume, neutron stress values show near zero at $Z=0.7$ mm and approximately 250 MPa near the top edge ($Z=11$ mm). As mentioned above, the contour and neutron measurements were conducted on different (nominally identical) specimens. Thus, the excellent agreement between the contour and neutron stress measurements also demonstrates a high degree of repeatability between the AM-Bench test specimens.

Figure 18 shows the longitudinal (X) residual stress values measured using the contour and neutron diffraction methods at $Y=2.5$ mm (mid-plane) at legs 4, 7, and 10 ($X=17$ mm, 31 mm, and 44 mm). Again, results show a high degree of agreement between the two methods. Variations in residual stresses between L4, L7, and L10 for the contour method are roughly equal to the those reported by neutron diffraction.

Residual Strain Comparison Between X-Ray and Neutron Diffraction

Since both neutron and X-ray diffraction techniques measured lattice spacings, it is more appropriate to directly compare residual strains instead of calculated stresses. This is especially true since the synchrotron X-ray approach could not measure all three orthogonal components that are needed to reliably calculate stresses. The direct comparison between neutron and X-ray results can only be made for the strains in the X and Z directions.

Figures 19 and 20 show the line profiles for ND and XRD for the X and Z strain components along the longitudinal (X direction) of the sample at various Z positions. Note that the XRD measurements were performed from $X=0$ mm to $X=75$ mm and ND measurements were performed from $X=0$ mm to $X=60$ mm. Figure 19 compares the longitudinal (X) strains at three different heights: near the top edge of the sample ($Z=11$ mm), near the middle of the top solid section ($Z=9.5$ mm), and through the legs of the sample ($Z=2.25$ mm). Since ND and XRD measurement positions do not align exactly, the orange lines of the plots indicate the ND longitudinal (X) strains and the blue and gray lines indicate the XRD strains at positions slightly above and below those of ND.

The longitudinal strains at all three Z heights exhibit a high degree of agreement between the XRD and the ND results. However, results near the edges of the sample once again reflect ND's inability to capture the large strain gradients. The higher effective spatial resolution of XRD (≈250 µm in the X direction) allows for strain measurements much closer to the edges of the sample. Near the left edge of the sample ($X=0$ mm), ND shows near zero longitudinal (X) strain, while XRD results consistently show a drastic change in strain from highly compressive (negative) to tensile (positive) from the left edge into the sample. XRD results near the sample edges were verified by confirming that the measurement gauge volumes were completely inside the part.

At $Z=2.25$ mm, the line profiles show the longitudinal (X) residual strains through the legs of the sample.

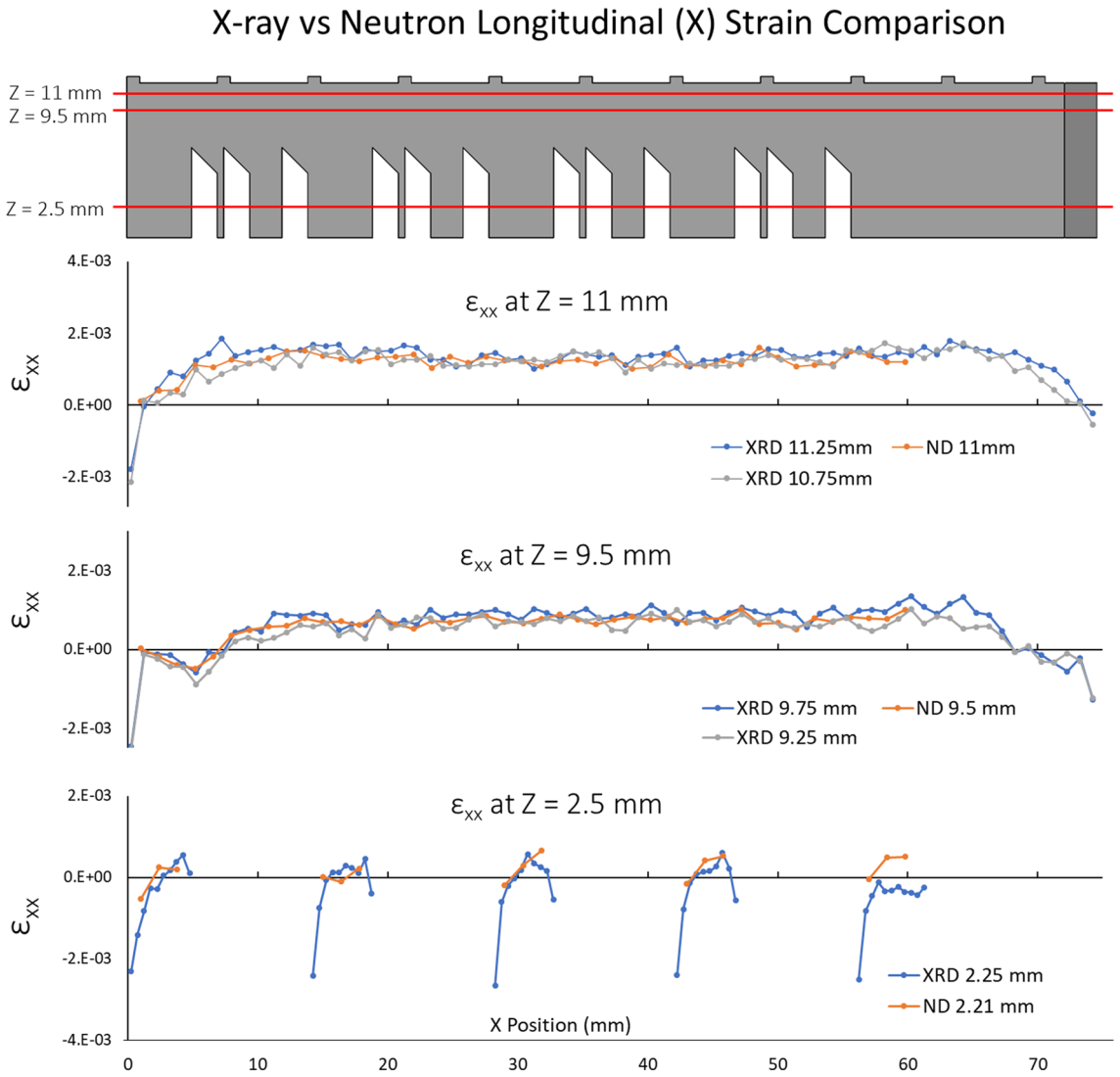

Fig. 19 Longitudinal (X) residual strain comparison between neutron and X-ray diffraction measurements. Line profiles of residual strains in the longitudinal (X) direction from XRD and ND are plotted near $Z = 11$ mm, 9.5 mm, and 2.25 mm. The top figure shows approximate locations of the residual strain line profiles for comparison

ND measurements were only performed through the thick leg sections. Again, the longitudinal strains correlate well between ND and XRD, except for near $X = 60$ mm. The difference between the measurements is roughly 5×10^{-4}. More generally, within these thicker leg sections, ND can only measure 3 positions, which does not show the complex strain variations within these legs. XRD results can better show the asymmetric strain distributions, ranging from high compression to mild tension and back to compression from one side to the other side of each leg.

Similar trends are observed between the XRD and ND strain results in the vertical/build (Z) direction. Figure 20 shows the line profiles for ND and XRD for the Z component of the elastic strain. ND results are plotted in orange, and XRD results are plotted in blue and gray at locations slightly above and below the ND measurement positions. The trend and magnitudes agree well between the two measurement techniques for positions near $Z = 11$ mm and 9.5 mm, although there appears to be a small consistent strain difference (approximately 4×10^{-4}) in the $Z = 11$ mm data. The difference in strain is slightly less than the uncertainty associated with the choice of the unstrained lattice parameter and translates to less than 60 MPa in stress.

For results at $Z = 2.25$ mm (through the legs measurements), the XRD vertical/build (Z) strains vary much more drastically compared with the X strains. XRD results show Z strains varying from highly tensile to highly compressive and then back to tensile from left to right of each leg. Due to the large fluctuation over a short distance, ND's gauge volume averaging effects are more noticeable. ND Z strains

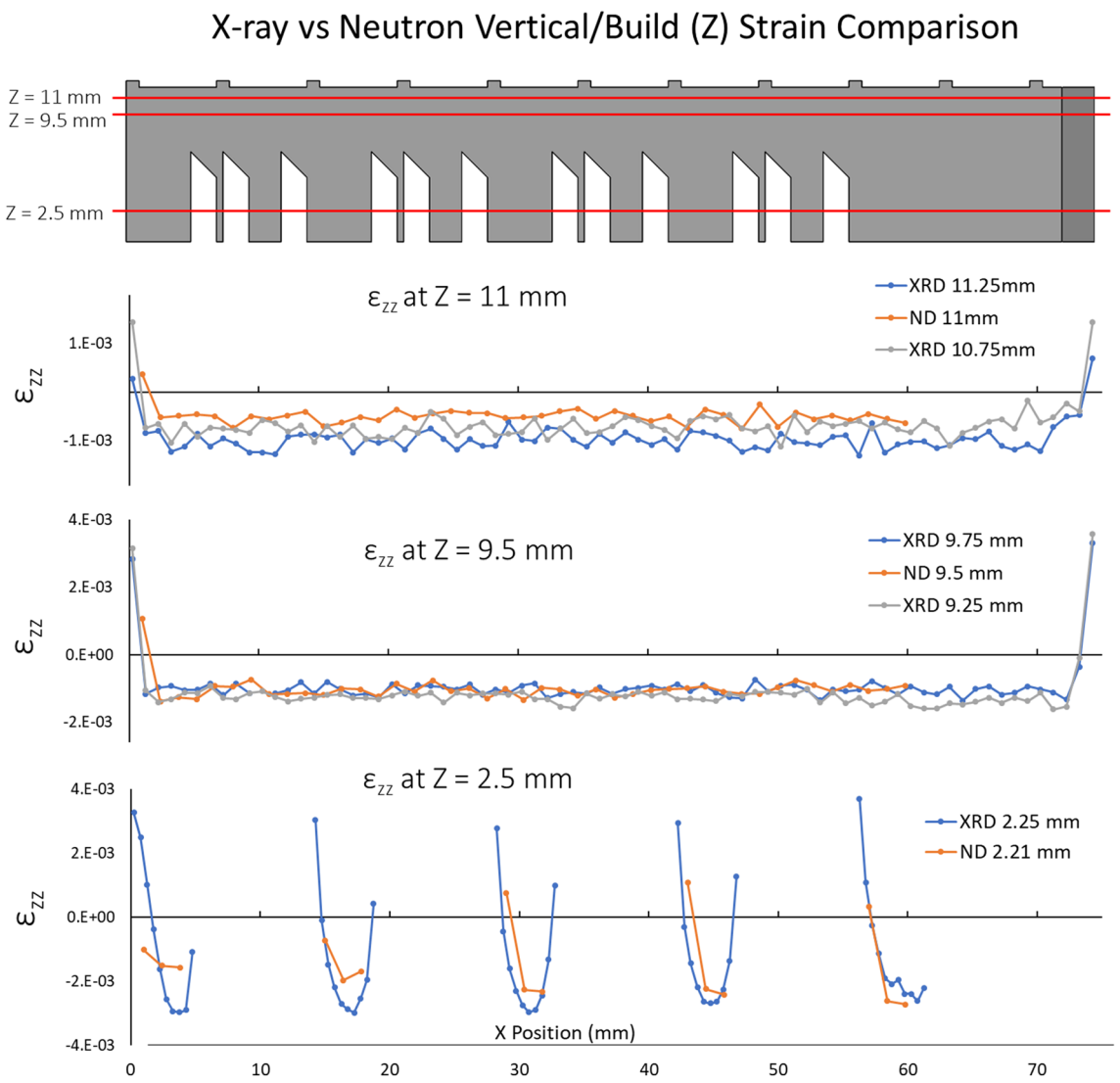

Fig. 20 Vertical/build (Z) strain comparison between neutron and X-ray diffraction measurements. Line profiles of residual strains in the vertical/build (Z) direction from XRD and ND are plotted at locations near $Z = 11$ mm, 9.5 mm, and 2.25 mm. The top figure shows approximate locations of the residual strain line profiles for comparison

indicate mostly compressive strains through the legs, unable to capture the highly tensile strains near the left edges of the large legs.

Conclusion and Summary

Residual strains and stresses of an as-built AM IN625 bridge-shaped structure have been measured using neutron diffraction, X-ray diffraction, and the contour method at various length scales. Vertical part deflections were measured using a CMM after the legs are separated from the build plate. Strains along three orthogonal directions (X, Y, and Z) were measured using neutron diffraction, with ≈ 1.5 mm spatial resolution. Strains along the X, Z, and 45° off Z directions were measured using synchrotron X-ray diffraction, with ≈ 250 μm spatial resolution. Residual stresses in the X direction were measured using the contour method for the part and build plate along three cross sections in the middle of legs 4, 7, and 10.

Comparisons of the results show excellent agreement between the techniques, with results showing high longitudinal (X) tensile strains on the top of the part. This is consistent with the upward deflection measured after the legs were separated from the build plate. X-ray diffraction results show highly tensile vertical/build (Z) strains and compressive longitudinal (X) strains near the edges of the sample and legs. Neutron diffraction was able to measure all three orthogonal strains in the X, Y, and Z directions, allowing for stress calculations at a large number of positions within the

Table 1 Summary of various residual strain/stress measurement techniques and their capabilities

Technique	Spatial resolution (m)	Destructive	Penetration	Complete strain/stress state
Neutron diffraction	10^{-3}	No[a]	High	Yes
X-ray diffraction	10^{-4}	No	Medium	No
Contour method	10^{-4}	Yes	N/A	No

[a]While neutron diffraction is a nondestructive technique, radiating the part can make it virtually unusable for a length of time depending on the half-life of the elements in the material

sample, which was not possible with the other techniques. However, for neutron diffraction, the assumption of the zero normal stress for the near surface neutron measurement may not provide an accurate strain-free lattice spacing since the measurement volume averages over a region which is stress-free (near the surface) and non-stress-free (1.5 mm below the surface). The effect of this systematic error was reflected in the observed differences in the two d_0 values calculated from the edge versus corner positions. However, the generally excellent comparison between all three techniques indicates that this deviation was small. Nevertheless, care should be taken in interpreting neutron results near the surface of the part if large gradients in strains/stresses exist over a small length scale. Part properties such as fatigue, which may depend on residual strains/stresses very close to the surfaces, might be better served using a higher-resolution technique such as XRD or the contour method.

These residual strain/stress measurement methods are complimentary in nature. The choice of technique depends on the sample size, material, and resolution requirements. When possible, multiple measurement techniques are recommended for the complete understanding of the residual strain/stress states within the AM parts. Table 1 provides a short summary comparing the measurement techniques and capabilities.

Acknowledgements Part of this research was supported by the Exascale Computing Project (17-SC-20-SC), a collaborative effort of the U.S. Department of Energy Office of Science and the National Nuclear Security Administration. Part of this work was performed under the auspices of the U.S. Department of Energy by Los Alamos National Laboratory, United States under Contract DE-AC52-06NA25396. Part of this work is based upon research conducted at the Cornell High Energy Synchrotron Source (CHESS) which is supported by the National Science Foundation under Award DMR-1332208. University of California, Davis, was supported by the Campus Executive program of Sandia National Laboratories.

Compliance with Ethical Standards

Conflict of interest On behalf of all authors, the corresponding author states that there is no conflict of interest.

References

1. Li C et al (2018) Residual stress in metal additive manufacturing. Procedia CIRP 71:348–353
2. Nadammal N et al (2017) Effect of hatch length on the development of microstructure, texture and residual stresses in selective laser melted superalloy Inconel 718. Mater Des 134:139–150
3. Robinson J et al (2018) Determination of the effect of scan strategy on residual stress in laser powder bed fusion additive manufacturing. Addit Manuf 23:13–24
4. Robinson JH et al (2018) The effect of hatch angle rotation on parts manufactured using selective laser melting. Rapid Prototyp J 25:289–298
5. Strantza M et al (2019) Directional and oscillating residual stress on the mesoscale in additively manufactured Ti-6Al-4 V. Acta Materialia 168:299–308
6. Levine LE et al (2019) Outcome and conclusions from the 2018 AM-bench measurements, challenge problems, modeling submissions, and conference. Integr Mater Manuf Innov (topical collection from the AM-bench 2018 test series)
7. Lass EA et al (2017) Formation of the Ni3Nb δ-phase in stress-relieved inconel 625 produced via laser powder-bed fusion additive manufacturing. Metall Mater Trans 48(11):5547–5558
8. Gnäupel-Herold T, Slotwinski J, Moylan S (2014) Neutron measurements of stresses in a test artifact produced by laser-based additive manufacturing. AIP Conf Proc 1581(1):1205–1212
9. Wang Z et al (2016) Diffraction and single-crystal elastic constants of Inconel 625 at room and elevated temperatures determined by neutron diffraction. Mater Sci Eng A 674:406–412
10. Gnäupel-Herold T (2012) ISODEC: software for calculating diffraction elastic constants. J Appl Crystallogr 45(3):573–574
11. Croft M et al (2002) Strain field and scattered intensity profiling with energy dispersive x-ray scattering. J Appl Phys 92(1):578–586
12. Croft M et al (2005) Strain profiling of fatigue crack overload effects using energy dispersive X-ray diffraction. Int J Fatigue 27(10):1408–1419
13. Tsakalakos T et al (2006) Measurement of residual stress distributions by energy dispersive X-ray diffraction synchrotron radiation. In: The sixteenth international offshore and polar engineering conference. International Society of Offshore and Polar Engineers, San Francisco, California, USA, p. 8
14. Strantza M et al (2018) Coupled experimental and computational study of residual stresses in additively manufactured Ti-6Al-4 V components. Mater Lett 231:221–224
15. High-density tungsten based metals—Mi-Tech metals. Available from: https://www.mttm.com/tungsten-alloys. Accessed 15 Apr 2019
16. Clausen B (2014) SMARTSware manual. Los Alamos National Lab, Los Alamos, NM, LA-UR 04-6581
17. Larson AC, Dreele RBV (1986) GSAS manual. Los Alamos National Lab, Los Alamos, NM, LA-UR 86-748
18. Holden TM, Suzuki H, Carr DG (2006) Macroscopic stress measurements by neutron diffraction and the part played by the "stress-free" reference. ISIJ Int 46(7):959–965

19. Prime MB, DeWald AT (2013) The contour method. In: Schajer GS (ed) Practical residual stress measurement methods. Wiley, Hoboken, pp 109–138
20. INCONEL alloy 625—special metals. Available from http://www.specialmetals.com/assets/smc/documents/alloys/inconel/inconel-alloy-625.pdf. Accessed 15 Apr 2019
21. Mahmoudi AH, Saei A (2015) Influence of asymmetrical cuts in measuring residual stresses using contour method. Int J Press Vessels Pip 134:1–10
22. Olson MD, DeWald AT, Hill MR (2018) Validation of a contour method single-measurement uncertainty estimator. Exp Mech 58(5):767–781